

Evidence for a cloud–cloud collision in Sh2-233 triggering the formation of the high-mass protostar object IRAS 05358+3543

Rin I. Yamada ¹★, Yasuo Fukui,² Hidetoshi Sano ^{3,4}, Kengo Tachihara ¹, John H. Bieging ⁵,
Rei Enokiya ⁶, Atsushi Nishimura ^{7,8}, Shinij Fujita ^{1,9}, Mikito Kohno ^{1,10} and Kiseitsu Tsuge ^{1,11}

¹Department of Physics, Nagoya University, Furo-cho, Chikusa-ku, Nagoya 464-8601, Japan

²Institute for Advanced Research, Nagoya University, Furo-cho, Chikusa-ku, Nagoya 464-8601, Japan

³Faculty of Engineering, Gifu University, 1-1 Yanagido, Gifu 501-1193, Japan

⁴National Astronomical Observatory of Japan, Mitaka, Tokyo 181-8588, Japan

⁵Steward Observatory, The University of Arizona, Tucson, AZ 85721, USA

⁶Department of Physics, Faculty of Science and Technology, Keio University, 3-14-1 Hiyoshi, Kohoku-ku, Yokohama, Kanagawa 223-8522, Japan

⁷Nobeyama Radio Observatory, National Astronomical Observatory of Japan (NAOJ), National Institutes of Natural Sciences (NINS), 462-2 Nobeyama, Minamimaki, Minamisaku, Nagano 384-1305, Japan

⁸Institute of Astronomy, the University of Tokyo, 2-21-1 Osawa, Mitaka, Tokyo 181-0015, Japan

⁹Department of Physical Science, Graduate School of Science, Osaka Prefecture University, 1-1 Gakuen-cho, Naka-ku, Sakai 599-8531, Japan

¹⁰Astronomy Section, Nagoya City Science Museum, 2-17-1 Sakae, Naka-ku, Nagoya, Aichi 460-0008, Japan

¹¹Dr. Karl Remeis Observatory, Erlangen Centre for Astroparticle Physics, Friedrich-Alexander-Universität Erlangen-Nürnberg, Sternwartstraße 7, D-96049 Bamberg, Germany

Accepted 2022 April 7. Received 2022 April 7; in original form 2021 May 11

ABSTRACT

We have carried out a new kinematical analysis of the molecular gas in the Sh2-233 region by using the CO $J = 2-1$ data taken at ~ 0.5 pc resolution. The molecular gas consists of a filamentary cloud of 5-pc length with 1.5-pc width where two dense cloud cores are embedded. The filament lies between two clouds, which have a velocity difference of 2.7 km s^{-1} and are extended over ~ 5 pc. We frame a scenario that the two clouds are colliding with each other and compressed the gas between them to form the filament in ~ 0.5 Myr which is perpendicular to the collision. It is likely that the collision formed not only the filamentary cloud but also the two dense cores. One of the dense cores is associated with the high-mass protostellar candidate IRAS 05358+3543, a representative high-mass protostar. In the monolithic collapse scheme of high mass star formation, a compact dense core of $100 M_{\odot}$ within a volume of 0.1 pc radius is assumed as the initial condition, whereas the formation of such a core remained unexplained in the previous works. We argue that the proposed collision is a step which efficiently collects the gas of $100 M_{\odot}$ into 0.1 pc radius. This lends support for that the cloud–cloud collision is an essential process in forming the compact high-mass dense core, IRAS 05358+3543.

Key words: stars: formation – ISM: clouds – ISM: individual objects: IRAS 05358+3543.

1 INTRODUCTION

High-mass star formation is an important process which substantially affects the galaxy evolution via enormous energy inputs into the interstellar medium (ISM). The energy inputs regulate the physical conditions of the ISM and control the gravitational collapse of the ISM which leads to high-mass star formation. The mechanism of high-mass star formation, however, has been an issue difficult to solve. The reason for this is multifold. The region of high-mass star formation is rare in the solar neighbourhood and detailed observations of this process were difficult as compared with the sites of low-mass star formation. Further, the time-scale of high-mass star formation is probably very short, less than Myr (e.g. Zinnecker & Yorke 2007), because of higher density of the star forming core, making a marked contrast with the low-mass star formation which

proceeds slowly in the order of 10 Myr due to low density (Jessop & Ward-Thompson 2000). Because of this contrast, there is a high barrier in finding out the high-mass star formation location and to resolve the star formation process therein with sufficient details. In spite of such difficulties, progress has been achieved by extensive surveys for massive dense cores, and hundreds of such cores have been catalogued in the Galactic plane (e.g. Beuther et al. 2010; Urquhart et al. 2014). Massive dense cores are believed to be precursors of high-mass stars because a high mass protostar should experience a massive dense core phase prior to a mature high-mass star. It is however not certain if all the massive cores are actual sites of high-mass star formation, since most of them lack a HII region, an unmistakable sign of high-mass stars emitting strong UV radiation. It was also puzzling that the number of such cores are large, suggesting a long time-scale like 10 Myr, leaving room to suspect that many of the cores, even if not all, may not be such precursors but stay stable as they are.

The observational difficulties may be overcome by theoretical works. McKee & Tan (2003) investigated typical density inherent to

* E-mail: yamada@phys.nagoya-u.ac.jp

the earliest phase of the high mass star formation in the literature, and found that many of the high mass star forming regions have common surface mass density around 1 g cm^{-2} , which corresponds to column density of $\sim 3 \times 10^{23} \text{ cm}^{-2}$. Cases of the high-column density in high-mass star formation include the massive clusters, the Orion Nebula Cluster in M42 and W3 Main, where around ten O stars are formed (for reviews O’Dell et al. 2008 and Megeath et al. 2008), as well as a more isolated high-mass protostar IRAS 05358+3543 in Sh2-233 (Beuther et al. 2007; see for a review Reipurth & Yan 2008). Krumholz et al. (2009) made hydrodynamical numerical simulations of gravitational collapse of a massive cloud core under the assumed initial condition, $100 M_{\odot}$ within 0.1 pc, corresponding to the condition found in the above regions. The simulations, which are usually referred to as the monolithic collapse models, successfully produced two $\sim 30 M_{\odot}$ stars in binary in a time-scale of a few times 10^4 yr, and showed that the issue of high mass star formation may be solved by the model.

It however remained to be explained how such a massive dense core can be formed in the ISM. The fact that such massive dense cores can form high-mass stars rapidly without fail suggests that the core may rapidly collapse to lower mass stars well before collected as a massive core. If one traces the whole gravitational collapse initiating by low density like 1000 cm^{-3} , the initial condition assumed by the monolithic collapse model might be hardly realized with self-gravity alone. This reasoning may be supported by the scenarios of a cloud–cloud collision in a number of star forming regions by the recent observational works including well-known HII regions M20, M42, and M17 (Torii et al. 2017; Fukui et al. 2018; Nishimura et al. 2018), giant molecular clouds with mini-starbursts W43, W51, and Carina (Fujita et al. 2021a,b; Kohno et al. 2021), the Galactic centre (Enokiya, Torii & Fukui 2021a; Tsuboi et al. 2021), the Magellanic Clouds (Fukui et al. 2017; Tsuge et al. 2019; Neelamkodan et al. 2021), M33 (Tokuda et al. 2020; Kondo et al. 2021; Sano et al. 2021), and the Antennae galaxies (Tsuge et al. 2021a,b) as well as theoretical results of colliding molecular gas flows (Inoue & Fukui 2013; Inoue et al. 2018; Fukui et al. 2020a). See also Fukui et al. (2020b) for a review of the related observational and theoretical works. Such colliding gas flows can significantly accelerate the gas collection by the supersonic motion, ten times faster than the free fall, without converting gas into stars, and may be a crucial step in forming a massive core.

In this paper, we intend to make a detailed kinematic study of the gas in the region of Sh2-233IR at ~ 10 arcmin to the south-east of Sh2-233, one of the representative cases of high gas surface density including the high mass protostar candidate IRAS 05358+3543. Fig. 1 shows a three-colour composite image of mid-infrared emission at 3.4, 12, and 22 μm obtained by *Wide-field Infrared Survey Explorer* (WISE) (Wright et al. 2010). The 3.4, 12, and 22 μm images mainly trace young stars, polycyclic aromatic hydrocarbon, and warm dust (Draine 2003; Draine et al. 2007; Carey et al. 2009). The 22 and 12 μm images are spatially correlated, and they show the spatial structure of HII regions around Sh2-233. The region shown in Fig. 1(a) harbours other HII regions Sh2-231, Sh2-232, and Sh2-235 in addition to Sh2-233 (see for a review Reipurth & Yan 2008), which are located at a distance of 1.8 kpc (Evans & Blair 1981) and within 40 pc of Sh2-233 on its eastern side in the galactic coordinate. This is a relatively dense region of star formation along the Galactic plane. It may be considered that these HII regions are expanding to accelerate the gas and triggering star formation in the surroundings according to a picture of Elmegreen & Lada (1977), because the HII regions can agitate the surrounding gas to accelerate expanding motions in a time-scale of several Myr or more, the probable duration

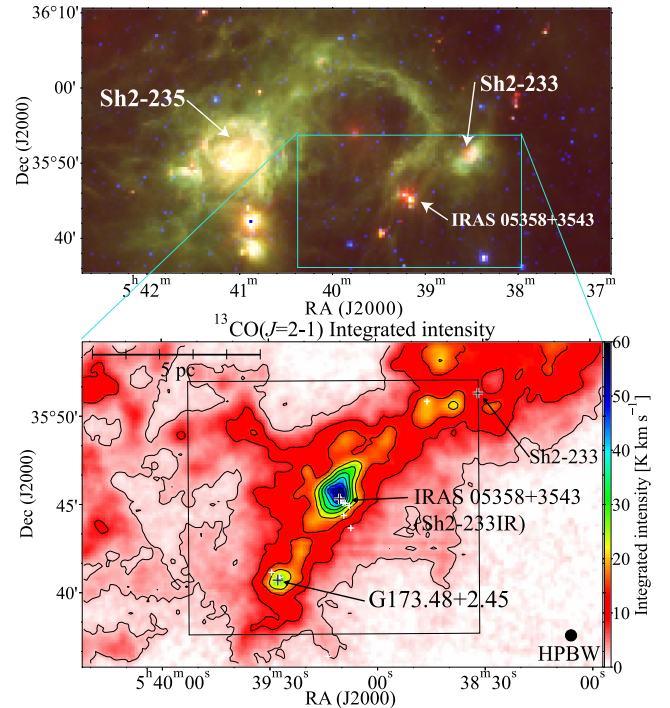


Figure 1. (a) Composite-colour image of the WISE 22 μm (red), 12 μm (green), and 3.4 μm (blue). The colour tables have been manipulated to emphasize the structural detail in the map (b) Integrated intensity distribution of the $^{13}\text{CO}(J=2-1)$ emission for a velocity range from -22 km s^{-1} to -12 km s^{-1} . Contours are plotted every 6 K km s^{-1} from 2 K km s^{-1} . The black crosses indicate the positions of Sh2-233, IRAS 05358+3543, and G173.58+2.45 corresponding to $(\alpha_{\text{J2000}}, \delta_{\text{J2000}}) = (05^{\text{h}}38^{\text{m}}31.5^{\text{s}}, 35^{\circ}51'19'')$, $(\alpha_{\text{J2000}}, \delta_{\text{J2000}}) = (05^{\text{h}}39^{\text{m}}10.4^{\text{s}}, 35^{\circ}45'19'')$, $(\alpha_{\text{J2000}}, \delta_{\text{J2000}}) = (05^{\text{h}}39^{\text{m}}27.7^{\text{s}}, 35^{\circ}40'43'')$, respectively. The white crosses show the positions of YSOs detected by Marton et al. (2016). The black rectangle outlines the region for which we obtained masses in Section 3.

of these extended HII regions. The active O star formation attracted attention and stimulated a number of works on star formation at multiwavelength. Most recently, a detailed analysis of the CO gas in Sh2-235 were carried out by Dewangan & Ojha (2017) (see the references therein for observational works at multiwavelength). This work suggests that a cloud–cloud collision is a viable mechanism of a recent trigger of star formation within a time-scale of Myr, whereas the acceleration of the gas clouds, which may be HI or H₂ clouds, could have originated more than a few Myr ago by acceleration due to HII regions.

This work is organized as follows; Section 2 summarizes the data used in the analysis and Section 3 the results of the analysis. Section 4 discusses the implications and Section 5 gives conclusions.

2 DATA SETS

We made use of the archival $J=2-1$ data of the ^{12}CO and ^{13}CO emission obtained with the Heinrich Hertz Submillimeter Telescope (SMT) at the Arizona Radio Observatory (Bieging et al. 2016). Entire observations were carried out by using the fully sampled on-the-fly (OTF) method with a full half-power beamwidth (HPBW) of 32 arcsec. The ^{12}CO and ^{13}CO data are both convolved to a spatial resolution of 38 arcsec. Both ^{12}CO and ^{13}CO data cubes were resampled to identical velocity grids with 0.15 km s^{-1} spacing by third-order interpolation. The typical noise fluctuations

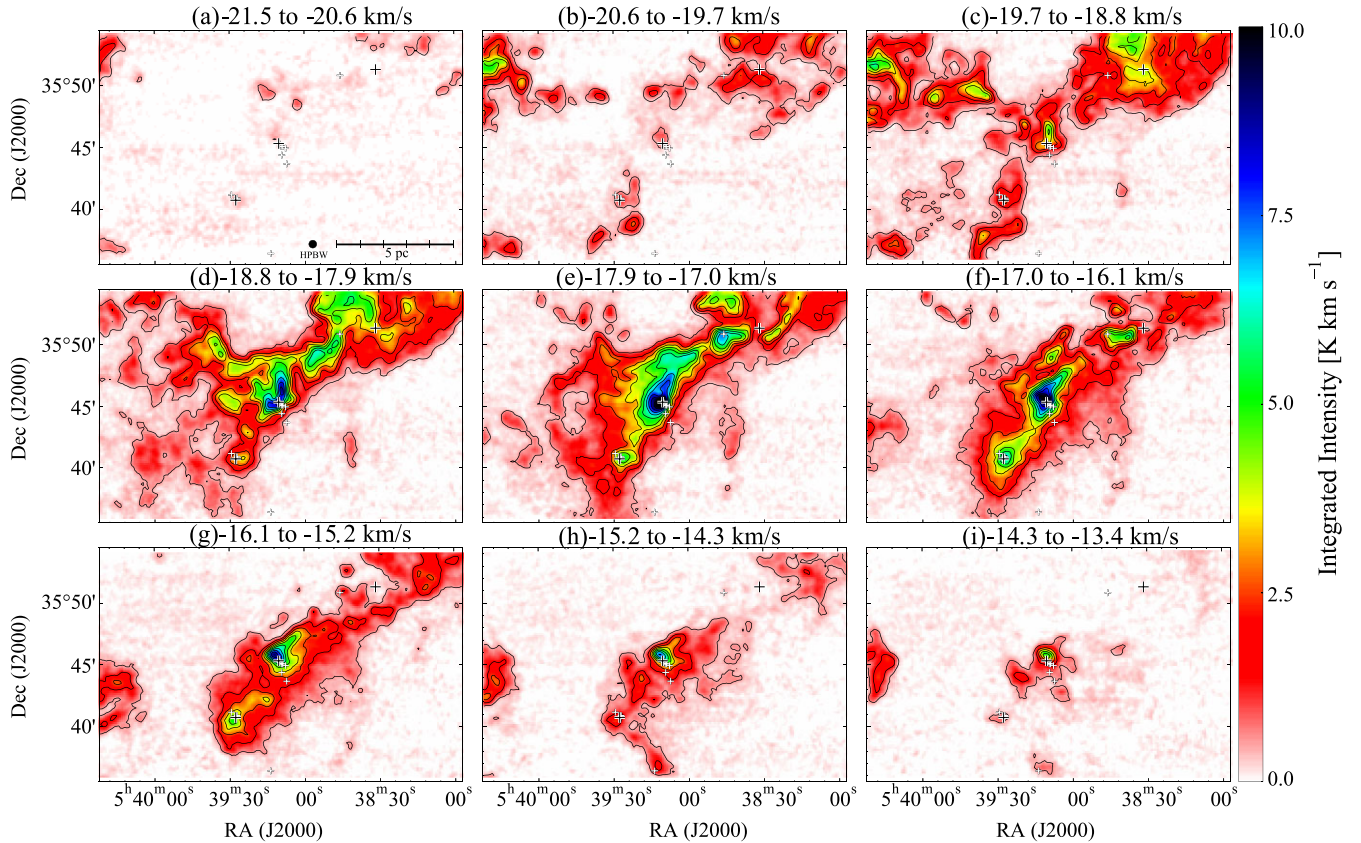


Figure 2. Velocity channel distribution of the $^{13}\text{CO}(J = 2-1)$ line emission. Integration velocity ranges are denoted at the top of each panel. Contours are plotted every 1 K km s^{-1} from 0.5 K km s^{-1} . The black crosses and white crosses are the same as Fig. 1.

are 0.10 K for ^{12}CO and 0.12 K for ^{13}CO at 0.15 km s^{-1} velocity grid. For more details of the observations, see Bieging et al. (2016).

3 RESULTS

3.1 Gas distribution towards the Sh2-233 region

The molecular gas in the Sh2-233 region has velocity in a range from -22 to -12 km s^{-1} . Fig. 1 shows the total integrated intensity of $^{13}\text{CO}(J = 2-1)$ in the velocity range. Hereafter, we shall use mostly $^{13}\text{CO}(J = 2-1)$ which is optically thin (see fig.18 of Bieging et al. 2016) and suited for tracing gas density. The molecular gas in the region shows filamentary distribution (hereafter ‘filament’) extending from the south-east to the north-west. Towards the brightest $^{13}\text{CO}(J = 2-1)$ peak at $(\alpha_{J2000}, \delta_{J2000}) \sim (05^{\text{h}}39^{\text{m}}12^{\text{s}}, 35^{\circ}45'40'')$, the high-mass protostar candidate IRAS 05358+3543 shown by a black cross and a few additional YSOs are located as shown by the white crosses (Marton et al. 2016). Another peak corresponding to G173.58+2.45 is located in the south-east at $(\alpha_{J2000}, \delta_{J2000}) \sim (05^{\text{h}}39^{\text{m}}30^{\text{s}}, 35^{\circ}40')$ and the third one at the north-west $(\alpha_{J2000}, \delta_{J2000}) \sim (05^{\text{h}}38^{\text{m}}45^{\text{s}}, 35^{\circ}40')$.

Fig. 2 shows velocity channel distributions of $^{13}\text{CO}(J = 2-1)$ ranging from -21.5 to -13.4 km s^{-1} every 0.9 km s^{-1} . Many panels show the filament with local peaks as substructures. The panels (a) to (e) show the blue-shifted component and the panel (g) to (i) show red-shifted component.

Fig. 3(a) shows the first moment of $^{13}\text{CO}(J = 2-1)$ where integrated intensity $>10 \text{ K km s}^{-1}$ is uniform at about -16 km s^{-1}

in the south-west, and that is uniform at around -18 km s^{-1} in the north-east. We find that there is a velocity difference of $\sim 2.6 \text{ km s}^{-1}$ between the south-western and north-eastern components within ~ 5 arcmin of the filament. Fig. 3(b) shows the second moment of $^{13}\text{CO}(J = 2-1)$, which is enhanced by a factor of 2–4 from 0.6 to 1.6 km s^{-1} towards the filament with a width of 1–2 pc. It seems that the red-shifted component is somewhat more localized in the α_{J2000} from $05^{\text{h}}38^{\text{m}}30^{\text{s}}$ to $05^{\text{h}}39^{\text{m}}20^{\text{s}}$ in panels (h) and (i) of Figs 2 and 3(a).

Fig. 4 shows typical CO profiles near Sh2-233IR in the three positions in Fig. 3(a) (A), (B), and (C). Figs 4(a) and (c) show single peaks which are blue-shifted in (a) and red-shifted in (c) and the peak velocity coincides with the first moment in Figs 3(a), and 4(b) shows a double peak (B) in both $^{12}\text{CO}(J = 2-1)$ and $^{13}\text{CO}(J = 2-1)$. Considering all of the above, we interpret that gas in the region of Sh2-233 consists of two different velocities towards the filament. We hereafter call the red-shifted component red cloud and the blue-shifted component blue cloud.

3.2 The red- and blue-shifted clouds

Here we consider the properties of the red and blue clouds in Sh2-233. First, we need to define the velocity ranges of the two clouds to obtain cloud properties, especially distribution and mass. However, in Sh2-233, the small velocity separation of approximately 2 km s^{-1} makes us hard to define the boundary velocity of the two clouds because spectra are merged at some pixels. Since these parameters strongly depend on the velocity range, it is crucial to define the velocity range using a reliable method.

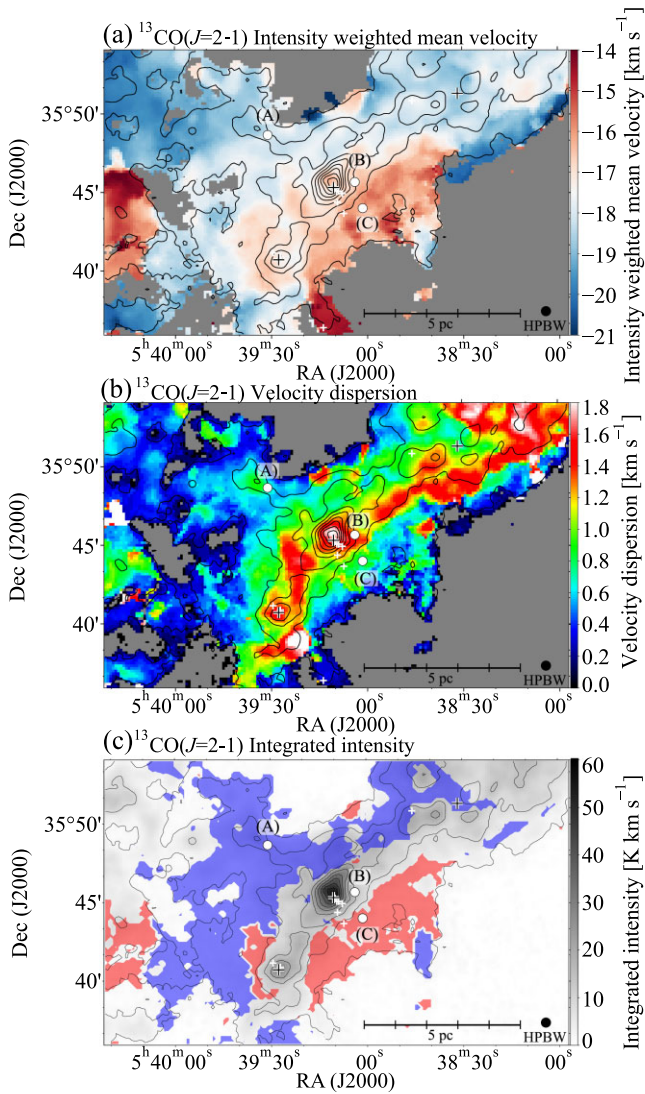


Figure 3. (a) Velocity centroid (the first moment) distribution of the $^{13}\text{CO}(J=2-1)$ emission. The calculation velocity range is from -22 to -12 km s^{-1} . Superposed contours show the integrated intensity distribution, same as Fig. 1. The black crosses and white crosses indicate the positions of Sh2-233, IRAS05358+3543, G173.58+2.45, and YSOs detected by Marton et al. (2016), respectively. White dots (A) to (C) indicates the position we present spectrum in Fig. 4. (b) Velocity dispersion (the second moment) distribution of the $^{13}\text{CO}(J=2-1)$ emission. Superposed contours are the same as (a). The black crosses and white crosses are the same as Fig. 1 (c) Same as Fig. 1(b) in grey scale. The red and blue shaded area indicate the determined area of the red and blue clouds, respectively.

A simple method using the first and second moment maps has been developed to separate multiple clouds in a region with complex velocity structure. The second moment is used to exclude areas where the spectra have multiple and/or merged peaks. In other words, by setting a threshold value of the second moment, we mask the areas where the second moment exceeds it. After removing the overlapping area, the first and second moments represent the cloud velocity centroid and the velocity dispersion. The method has been applied to separate merging two clouds in the Orion region (M42/43; Fukui et al. 2018, NGC 2024; Enokiya et al. 2021b, NGC 2023; Yamada et al. 2021) as well as the Galactic Centre region having more complicated velocity structures (Enokiya et al. 2021a)

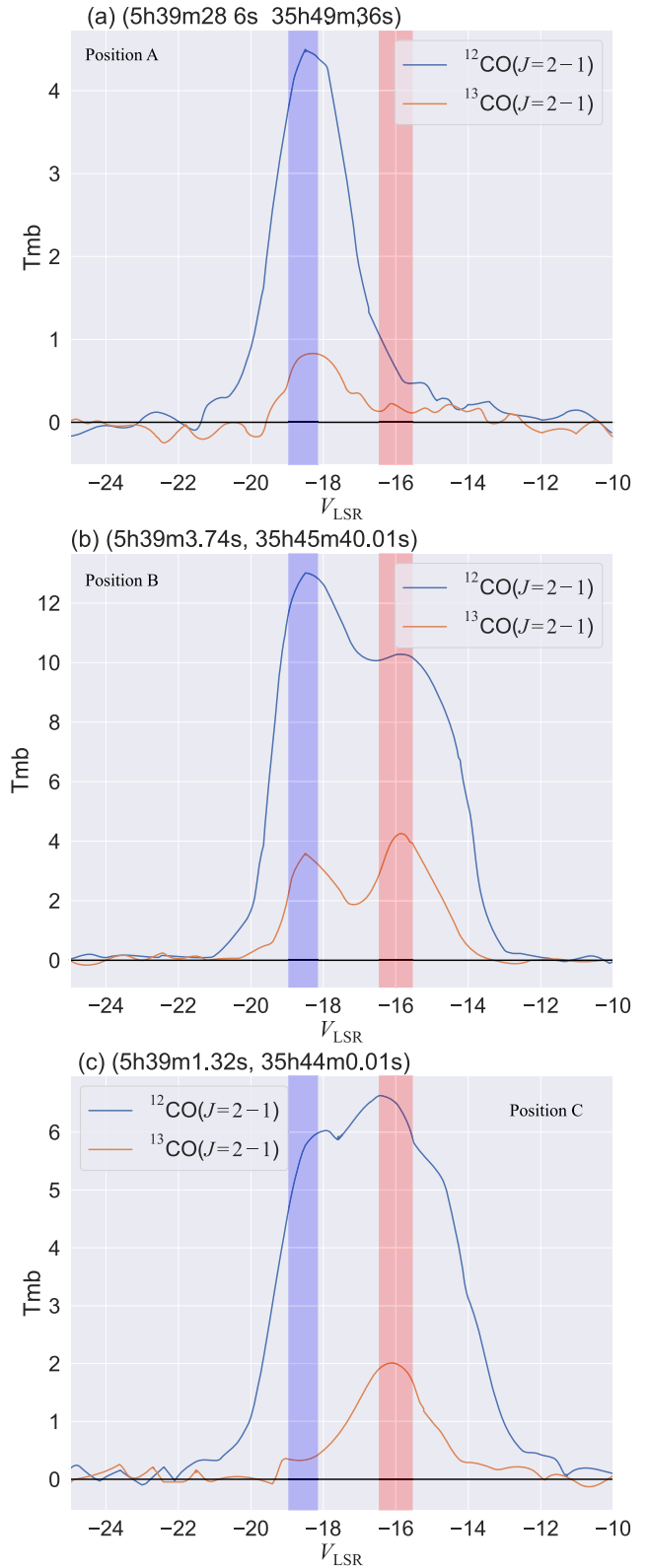


Figure 4. $^{12}\text{CO}(J=2-1)$ and $^{13}\text{CO}(J=2-1)$ spectra at the position (a) to (c) in Fig. 3. The red and blue bands show the representative velocity ranges of each cloud defined in Section 3.

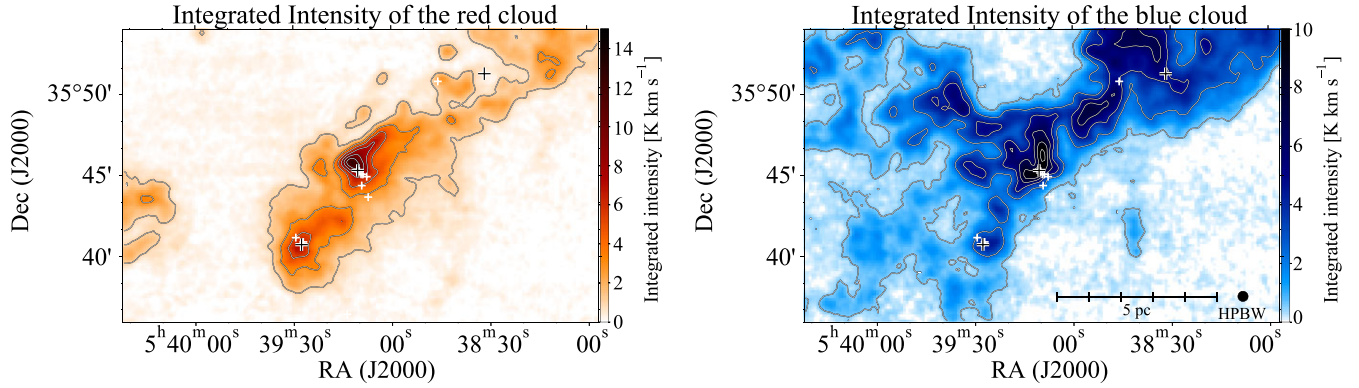


Figure 5. (a) Integrated intensity distribution of the red cloud. The integration range is from -15.4 to -16.5 km s^{-1} . Contours are plotted every 2 K km s^{-1} from 0.5 K km s^{-1} . (b) Integrated intensity distribution of the blue cloud. The integration range is from -19.1 to -18.2 K km s^{-1} . The lowest contour and contour intervals are the same as (a). The black crosses and white crosses are the same as Fig. 1.

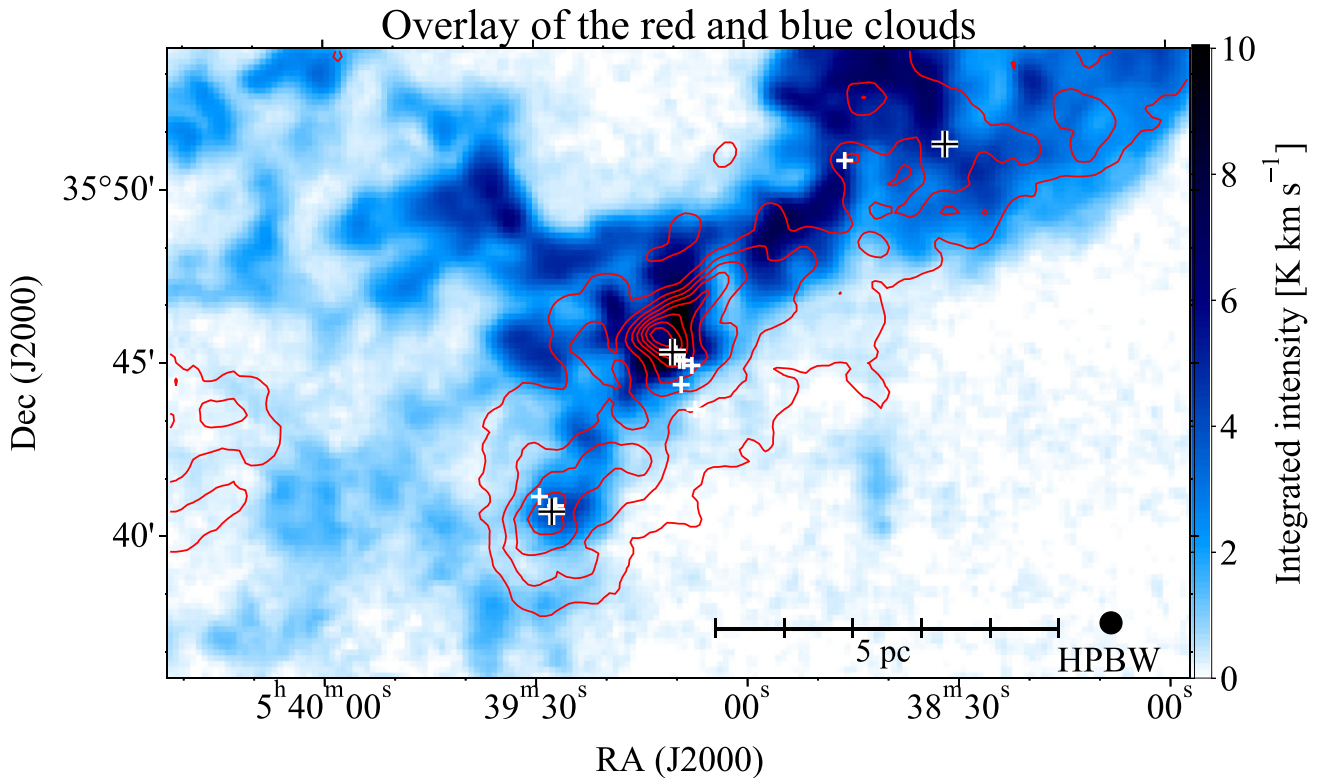


Figure 6. $^{12}\text{CO}(J=2-1)$ integrated intensity distribution of the red and blue clouds. The integration velocity range is from -15.4 to -16.5 km s^{-1} for the image; -19.1 to -18.2 km s^{-1} for the contours. The black crosses and white crosses are the same as Fig. 1.

In the Sh2-233 region, we obtained the velocity ranges as follows:

(i) We checked every spectrum by eye and found that the spectra have multiple or merged peaks in the area with the second moment higher than 1.0 km s^{-1} .

(ii) We exclude the areas with the second moment higher than the threshold value.

(iii) We define the regions of the red and blue clouds as the first moment >-17 and <-17 km s^{-1} , respectively. The regions are outlined by red and blue shades in Fig. 3(c).

(iv) We average the values of the first and second moments within the defined regions.

The velocity range for the red cloud is defined as from $V_{\text{representative, red}} - dV_{\text{red}}$ to $V_{\text{representative, red}} + dV_{\text{red}}$ and the veloc-

ity range for the blue cloud as from $V_{\text{representative, blue}} - dV_{\text{blue}}$ to $V_{\text{representative, blue}} + dV_{\text{blue}}$, where $V_{\text{representative, red}}$, $V_{\text{representative, blue}}$, dV_{red} , dV_{blue} are -15.92 , -18.63 , 0.48 , 0.53 km s^{-1} , respectively.

We have checked the validity of the method in Sh-233 by spectral decomposition by multicomponent Gaussian fitting. For details, see appendix A. By applying these criteria we derived the representative velocity range of the blue cloud to be -19.1 to -18.2 km s^{-1} , and that of the red cloud to be -16.5 to -15.4 km s^{-1} . Fig. 5 shows the distributions of the red and blue clouds, and the two clouds are both peaked towards IRAS 05358+3543. Fig. 6 shows an overlay of the two clouds, confirming that the filamentary distribution coincides with the area where the two clouds are overlapping. We also find that the blue cloud has a sharp intensity drop to the south-west and is extended to the north-east with another filamentary feature extending

Table 1. Physical parameters of the molecular clouds.

Cloud name	Column density (cm^{-2})	Mass (M_{\odot})
(1)	(2)	(3)
Filament	2.2×10^{22}	1030
Red cloud	1.3×10^{22}	580
Blue cloud	1.9×10^{22}	840

Note. Col.(1) Cloud name. Col.(2) The peak column density of each cloud/filament. Col.(3) Masses derived by assuming the local thermodynamical equilibrium in α_{J2000} and δ_{J2000} ranges of $05^{\text{h}}38^{\text{m}}31^{\text{s}}-05^{\text{h}}39^{\text{m}}12^{\text{s}}$ and $35^{\circ}37'30''-35^{\circ}51'46''$, respectively. For the filament, we used the region enclosed by a third-lowest contour corresponding to 14 K km s^{-1} in Fig. 1. For the red/blue cloud, the mass is derived by the region where the first moment is larger/smaller than -17 km s^{-1} and the second moment is smaller than 1.0 km s^{-1} in a velocity range from -22 to -12 km s^{-1} in Fig. 3. For more details of the method, see Enokiyama et al. (2021b). Note that we only use voxels with intensity higher than $5 \times T_{\text{rms}} = 0.6 \text{ K}$ in Col.(2)–(3).

to the north from the IRAS 05358+3543 core. In contrast to the blue cloud, the red cloud is extended to the south-east with a relatively sharp drop towards the north-east.

3.3 The physical properties of the clouds

By assuming the local thermodynamical equilibrium, we derived the column density of the molecular gas. We estimated T_{ex} in each pixel, assuming that the $^{12}\text{CO}(J=2-1)$ line is optically thick. Then the $^{13}\text{CO}(J=2-1)$ optical depth and the ^{13}CO column density were calculated from the radiative transfer equation. The abundance ratio of H_2 to ^{13}CO is assumed to be 5.0×10^5 (Dickman 1978). The results are given in Table 1.

We estimated the total molecular mass to be $2440 M_{\odot}$ in the region outlined by the black rectangle in Fig. 1(b) and in the velocity range from -22 to -12 km s^{-1} . For the red and blue clouds, we derived the masses in the regions determined by the moment method as described in section 3.2 (See Fig. 3c). The filament is prominent in the area where the integrated intensity is higher than 14 K km s^{-1} , corresponding to the third lowest contour in Fig. 1(b). We estimated the filament mass to be $1030 M_{\odot}$ in the region enclosed by the third-lowest contour. Although the red and blue clouds and the filament are defined by different methods, they are distributed exclusively, and the sum of these three masses is consistent well with the total molecular mass of $2440 M_{\odot}$.

3.4 The molecular outflows associated with IRAS 05358+3543 and G173.58+2.45

Two molecular outflows were detected in the $^{12}\text{CO}(J=1-0)$ emission towards IRAS 05358+3543 and G173.58+2.45 by Snell, Dickman & Huang (1990) and Shepherd & Churchwell (1996), respectively. Figs 7 and 8 show their spatial distributions of the $^{12}\text{CO}(J=2-1)$ and $^{13}\text{CO}(J=2-1)$ outflow wings and typical profiles in the present data. The velocity ranges and the other physical parameters including size, outflow velocity, mass, dynamical time-scale, mass-loss rate, and outflow momentum are calculated for a detection limit of $5 \times T_{\text{rms}}$ under an assumption of intensity ratio of the $^{12}\text{CO}(J=2-1)/^{12}\text{CO}(J=1-0)$ of 0.8 by referring to the $^{12}\text{CO}(J=1-0)$ emission (Shepherd & Churchwell 1996) where the same as assumed in IRAS 05358+3543.

The X_{CO} factor is assumed to be $1.0 \times 10^{20} [(\text{K km s}^{-1})^{-1} \text{ cm}^{-2}]$ (Okamoto et al. 2017) for the two objects. The results listed in Table 2 are basically consistent with the previous observations, while the size of the IRAS 05358+3543 outflow was found to be a factor of about two smaller than that in Snell et al. (1990). This could be due to the higher resolution of the present data 38 arcsec than that by Snell et al. (1990), who adopted a grid spacing of $1-1.5 \text{ arcmin}$ with a 45 arcsec beam.

4 DISCUSSION

4.1 Triggered star formation in the Sh2-233 region

As presented in section 3.2, the Sh2-233 region has two velocity components with a velocity difference of 2.7 km s^{-1} . We discuss if the velocity separation were created by the feedback effect of molecular outflows by young stars or by the HII regions.

Molecular outflows can affect cloud kinematic motion via momentum transfer. In general, outflow velocity is supersonic, larger than 10 km s^{-1} . The dynamical effect of an outflow is limited to the inner areas of the outflow lobes, where gas particles are moving away from the driving central star. In case of the present region, the two molecular outflows having sizes of less than $\sim 1 \text{ pc}$ are associated with IRAS 05358+3543 and G173.58+2.45, respectively (Table 2). Ginsburg et al. (2009) found that shock excited H_2 emission is localized in a 0.5 pc radius centred at IRAS 05358+3543. Since the sizes of the two outflows are smaller than 1 pc , it is unlikely that the velocity separation of the two clouds extending more than 5 pc can be explained by the molecular outflows.

Another possible cause of the velocity separation is expanding HII regions. Sh2-233 and Sh2-233IR are associated with HII regions whose size is less than 1 pc , much smaller than the extent of the two clouds. Here we roughly estimate the radius of shock front driven by the HII region. The typical propagation velocity of the ionization front in the molecular gas is $\sim 5 \text{ km s}^{-1}$ (Elmegreen & Lada 1977), and the age of Sh2-233 is estimated to be less than 1 Myr (Ladeyschikov et al. 2015). Thus, the radius of the shock front driven by the HII region is $\sim 0.2 \text{ pc}$, which is significantly smaller than 5 pc . This implies that the velocity separation cannot be originated from the expanding motion of the HII region Sh2-233. In addition, we find no particularly broad linewidth towards the two protostellar sources in Fig. 3(b), while we see somewhat broad linewidth along the filament in the direction both on and off the outflow sources/HII regions. In summary, we consider that the stellar feedback is negligible as the cause of the velocity separation, and the velocity distribution of the present two clouds exist prior to the star formation in the filament.

An alternative idea to explain the velocity separation is a cloud–cloud collision. A typical signature of a cloud–cloud collision is intermediate velocity components connecting the two clouds in the velocity space (Fukui et al. 2020b), namely the bridge feature, which is seen in the Sh2-233 region. The bridge feature is produced by momentum exchange as collision proceeds. In other words, each cloud is decelerated by collision, and we observe the intermediate velocity components as a bridge feature in the position–velocity diagram. Figs 9(b)–(j) show position–velocity diagrams integrated along the Y-OFFSET axis, indicating the bridge feature connecting the two components. This distribution is interpreted as a piece of evidence of cloud merging due to the collision, where the intermediate velocity gas is produced in the interface layer where gas is decelerated. Fig. 9(f) shows a faint $^{13}\text{CO}(J=2-1)$ feature localized at X-OFFSET ~ 0 outside of the velocity range from -21

Table 2. Physical parameters of the molecular outflows.

Lobe name	Size (pc)	V_{sys} (km s^{-1})	V_{outflow} (km s^{-1})	Mass (M_{\odot})	t_{dyn} (Myr)	Mass loss rate ($M_{\odot} \text{ yr}^{-1}$)	Momentum ($\text{km s}^{-1} M_{\odot}$)
(1)	(2)	(3)	(4)	(5)	(6)	(7)	(8)
IRAS 05358+3543 blue lobe	0.73	−16.1	12.3	44	0.14	3.1×10^{-4}	541
IRAS 05358+3543 red lobe	0.56	−16.1	10.5	28	0.12	2.3×10^{-4}	294
G173.58+2.45 blue lobe	0.71	−16.7	12.9	53	0.13	4.0×10^{-4}	683
G173.58+2.45 red lobe	0.98	−16.7	10.8	48	0.23	2.0×10^{-4}	518

Note. Col. (1) Lobe name. Col. (2) Effective diameters defined by $(A/\pi)^{1/2} \times 0.5$, where A is the region enclosed by the lowest contours in Figs 7(a) and 8(a). Col. (3) Systemic velocities defined as peak velocities of $^{13}\text{CO}(J=2-1)$. Col. (4) Three-sigma level maximum radial velocity of the outflow lobe with respect to the systemic velocity. Col. (5) Masses of the lobes. Col. (6) Dynamical time-scale derived by dividing the two most distant points on the lowest contour by V_{outflow} . Col. (7) Mass-loss rate derived by $\text{Mass}/t_{\text{dyn}}$. Col. (8) Momentum estimated by $\text{Mass} \times V_{\text{outflow}}$.

to -14 km s^{-1} (Fig. 9f). This is possibly ascribed to part of the outflow wings (Fig. 7).

The red and blue clouds are overlapped towards Sh-233IR and G173.58+2.45. We find that the blue cloud shows asymmetry relative to the cloud ridge in the sense that the gas is extended to the north-east (see Fig. 6), while there is little gas distributed in the south-west. The asymmetry is explained as due to sweeping up of the initially extended gas distribution by collision with the red cloud, and the compressed gas column density amounts to $2.2 \times 10^{22} \text{ cm}^{-2}$. A similar, less pronounced asymmetry in the opposite sense is found in the red cloud that has extended gas in the south-west of the filament, which may be explained by a similar sweeping up on the opposite side. It is possible that the low-density gas in the two clouds was compressed and condensed into the filamentary cloud within $\sim 1 \text{ Myr}$, the collision time scale as shown below. So, the large-scale gas distribution at $\sim 5 \text{ pc}$ seems also to be consistent with the collision picture.

Finally, we argue that the time-scale of cloud–cloud collision is also roughly consistent with the age of the star cluster. According to Porras, Cruz-González & Salas (2000), the stellar age upper limit in the IRAS 05358+3543 region is $\sim 3 \text{ Myr}$. Detailed age discussion is given in section 4.2. The collision time-scale, which is often expressed as a cloud crossing time, is $\sim 5 \times 10^5 \text{ yr}$ ($= 1.5 \text{ pc}/2.7 \text{ km s}^{-1}$). Both the red and blue clouds show elongated structures from south-east to north-west, so it is reasonable to derive the cloud crossing time by dividing a cloud width of 1.5 pc^1 by the velocity separation of 2.7 km s^{-1} . The time-scale varies depending on the assumed angle from 5×10^5 to $8 \times 10^5 \text{ yr}$ for a range of angle from 30 to 60 deg. The main spatial range of the collision is from $38^{\text{m}}50^{\text{s}}$ to $39^{\text{m}}40^{\text{s}}$ in RA and from $35^{\circ}38'$ to $39^{\circ}48'$ in Dec because the two components are clearly seen in the position–velocity diagram. The collision between the two clouds compressed the interface layer to form the filamentary cloud over $\sim 5 \text{ pc}$ in the direction perpendicular to the collision direction. It seems the collision produced at least the two cores towards Sh2-233IR and G173.58+2.45 nearly synchronously.

4.2 The two regions of recent star formation triggered by the cloud–cloud collision

The most active star formation as indicated by more than 10 molecular outflows within 1 pc (Ginsburg et al. 2009) is taking

¹The cloud width of 1.5 pc is an average full-width half-maximum (FWHM) value of five strips perpendicular to the filament (along X-OFFSET in Fig. 9). The FWHM values are derived by Gaussian fitting.

place in the core towards Sh2-233IR where IRAS 05358+3543 is located. The core has an effective radius r_{eff} of 0.4 pc and its mass is estimated to be $230 M_{\odot}$. The masses are derived by summing the column densities over the areas enclosed by a contour at the half of the peak column densities. We described details in appendix C. Porras et al. (2000) made *JHK* photometric observations of Sh2-233IR and identified two clusters NE and SW, which are separated with each other by 0.5 pc in the direction perpendicular to the filament. The NE cluster on the filament is significantly redder than the SE cluster, which is more exposed and shifted to the south-west from the filament. IRAS 05358+3543 is most likely a member of the cluster NE and the associated outflow has a dynamical age of $\sim 10^4 \text{ yr}$. This dynamical age is shorter than the collision time-scale of $(5-8) \times 10^5 \text{ yr}$, which is consistent with the numerical simulations of colliding clouds (Fukui et al. 2020a), and does not contradict the stellar age upper limit, 3 Myr (Porras et al. 2000).

The observational properties of the cores and numerical simulations in the literature agree with each other. Inoue & Fukui (2013) performed a 3D magnetohydrodynamic (MHD) numerical simulation of two colliding clouds. They showed that clouds are compressed into filamentary features having a typical width of 0.1 pc, and dense cores with masses of more than $100 M_{\odot}$ are formed without being consumed for low-mass star formation due to enhanced turbulence and magnetic field. Takahira, Tasker & Habe (2014) simulated two colliding clouds having different sizes and showed the gravitationally bound cores are formed in the shock-compressed layer. Besides these, high resolution numerical calculation (Takahira et al. 2018) as well as those include effects of magnetic fields (Inoue et al. 2018; Sakre et al. 2021) showed that cloud–cloud collisions compress gas into gravitationally bound cores. Fukui et al. (2020a) made a detailed investigation of the cores simulated in Inoue & Fukui (2013) and found that the typical diameters and masses of the cores are 0.05 pc and $30 M_{\odot}$, respectively. Sh2-233IR has sub-mm/mm cores resolved into several dust condensations mm1a-b, mm2a-d, mm3, mm4 several of which have protostellar nature (Larionov et al. 1999; Beuther et al. 2002, 2007; Leurini et al. 2007; Colzi et al. 2019). Typical diameters and masses are 0.05 pc and $10 M_{\odot}$, respectively. In addition, the sub-mm/mm core mm1a is likely associated with the 1.3 mm continuum emission, extending in the same direction with the filament at a 1 pc scale.

A question arising is if the formation of the cluster is due to the gravitational instability in the filamentary cloud and the gas flow along the filament collects the mass into the cluster. We suggest that the cluster formation is more strongly influenced by the initial density distribution prior to the filament formation than the flow along the filament, and dominated by the dynamical compression in the collision. This is because the column density of the blue

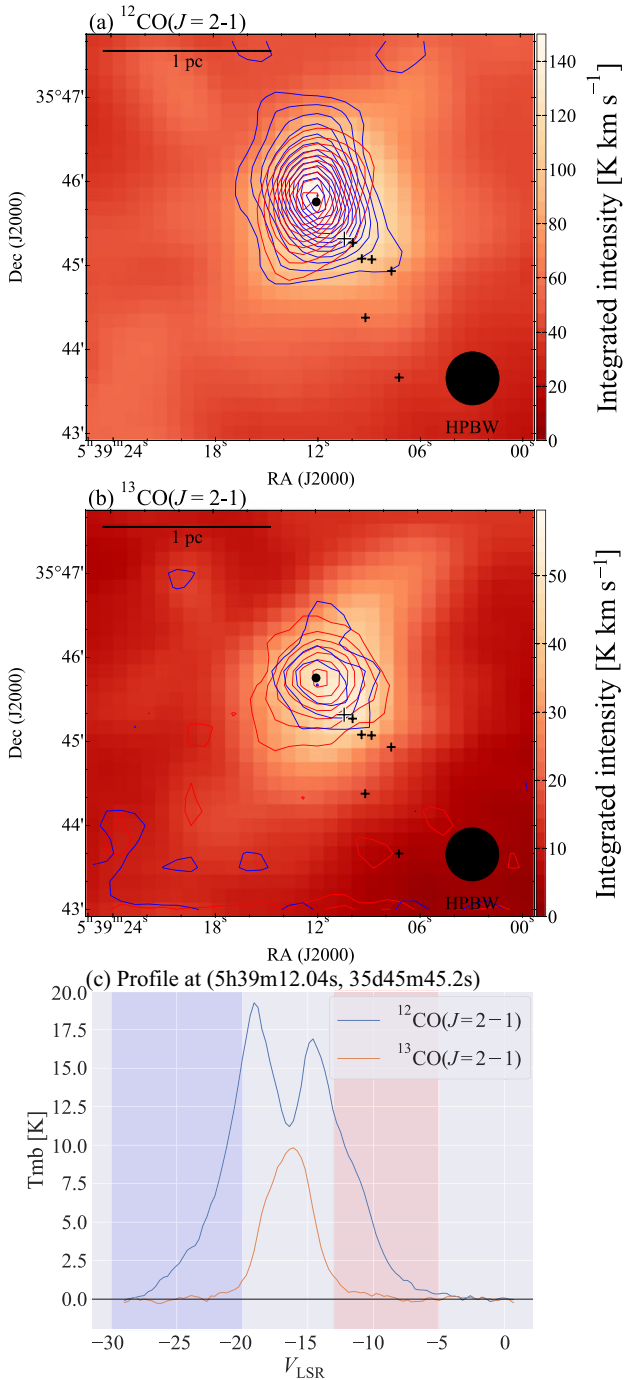


Figure 7. (a) Spatial distributions of the outflow associated with IRAS 05358+3543 in $^{12}\text{CO}(J=2-1)$. Image shows the integrated intensity distribution of the $^{12}\text{CO}(J=2-1)$ emission for a velocity range of -22 to -12 km s^{-1} . The red and blue contours are plotted every 2 from 9 K km s^{-1} . Contour levels are selected to avoid a significant contamination by ambient gas. Integration velocity range is from -30 to -21 km s^{-1} for the blue wing; from -12 to -6 km s^{-1} for the red wing, which are shown by blue and red transparent bands in (c), respectively. (b) Same as (a), but in $^{13}\text{CO}(J=2-1)$. Image shows the integrated intensity distribution of the $^{13}\text{CO}(J=2-1)$ emission for a velocity range of -22 to -12 km s^{-1} . The red and blue contours are plotted every 0.5 from 0.5 K km s^{-1} . The black dot shows the position we present typical velocity profile in (c). Larger black cross and smaller black crosses indicate the positions of IRAS 05358+3543, YSOs (Marton et al. 2016), respectively. (c) Line profile at the position shown by the black dot in (a).

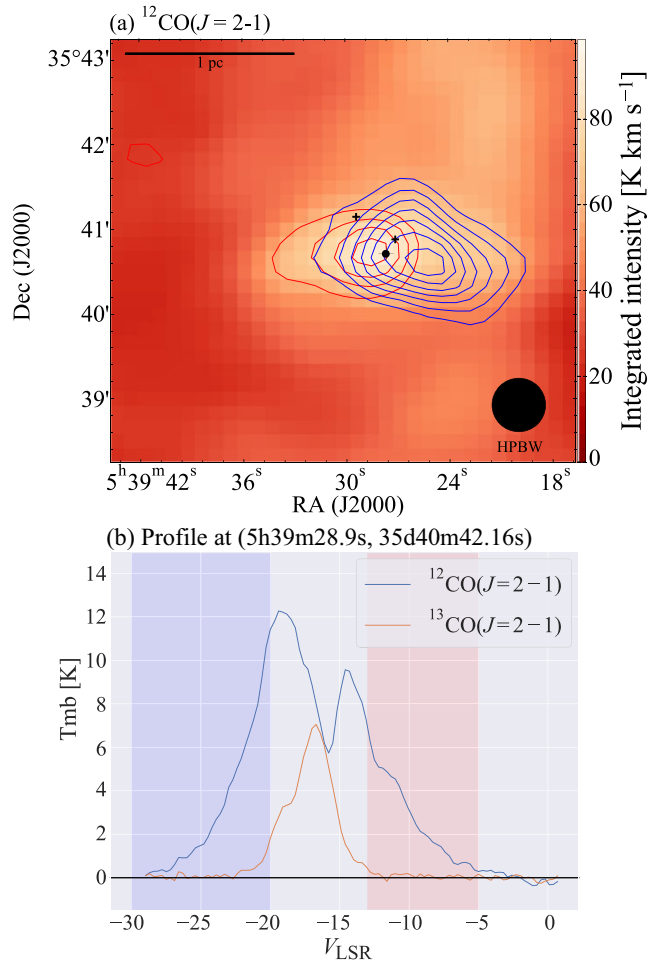


Figure 8. (a) Spatial distributions of the outflow associated with G173.58+2.45 in $^{12}\text{CO}(J=2-1)$. Image shows the integrated intensity distribution of the $^{12}\text{CO}(J=2-1)$ emission for a velocity range of -22 to -12 km s^{-1} . The red and blue contours are plotted every 3 K km s^{-1} from 6 K km s^{-1} . Contour levels are selected without making a significant contamination by ambient gas. Integration velocity range is from -30 to -21 km s^{-1} for the blue wing; from -13 to -5 km s^{-1} for the red wing, which are shown by blue and red transparent bands in b, respectively. The black crosses indicate the positions of YSOs (Marton et al. 2016). (b) Line profile at the position shown by the black dot in (a).

cloud is enhanced in the northeast of the Sh2-233IR and by the collision the enhanced density will increase the core mass more rapidly than in the rest of the filament. Fig. 10 shows two strips along and perpendicular to the filament including the two cores and clearly shows that the column density is enhanced at X-OFFSET = 0.0. We suggest that the enhancement of the blue cloud in column density as indicated by the cloud extended to the north favoured the formation of the Sh2-233IR core, and thereby the formation of IRAS 05358+3543.

The G173.58+2.45 core is associated with IRAS 05361+3539 and an ultracompact HII region. CO outflow is driven by a late B or mid A star (Shepherd & Churchwell 1996) in a small cluster of Class I and II sources (Chakraborty et al. 2000; Shepherd & Watson 2002; Varricatt, Davis & Adamson 2005), H_2O masers (Wouterloot & Brand 1989; Palagi et al. 1993), and H_2 emission shocks (Chakraborty et al. 2000; Varricatt et al. 2005).

Another core is towards the HII region Sh2-233 having a B1 star (Hunter and Massey 1990) with an age of 10^5 yr and is associated with

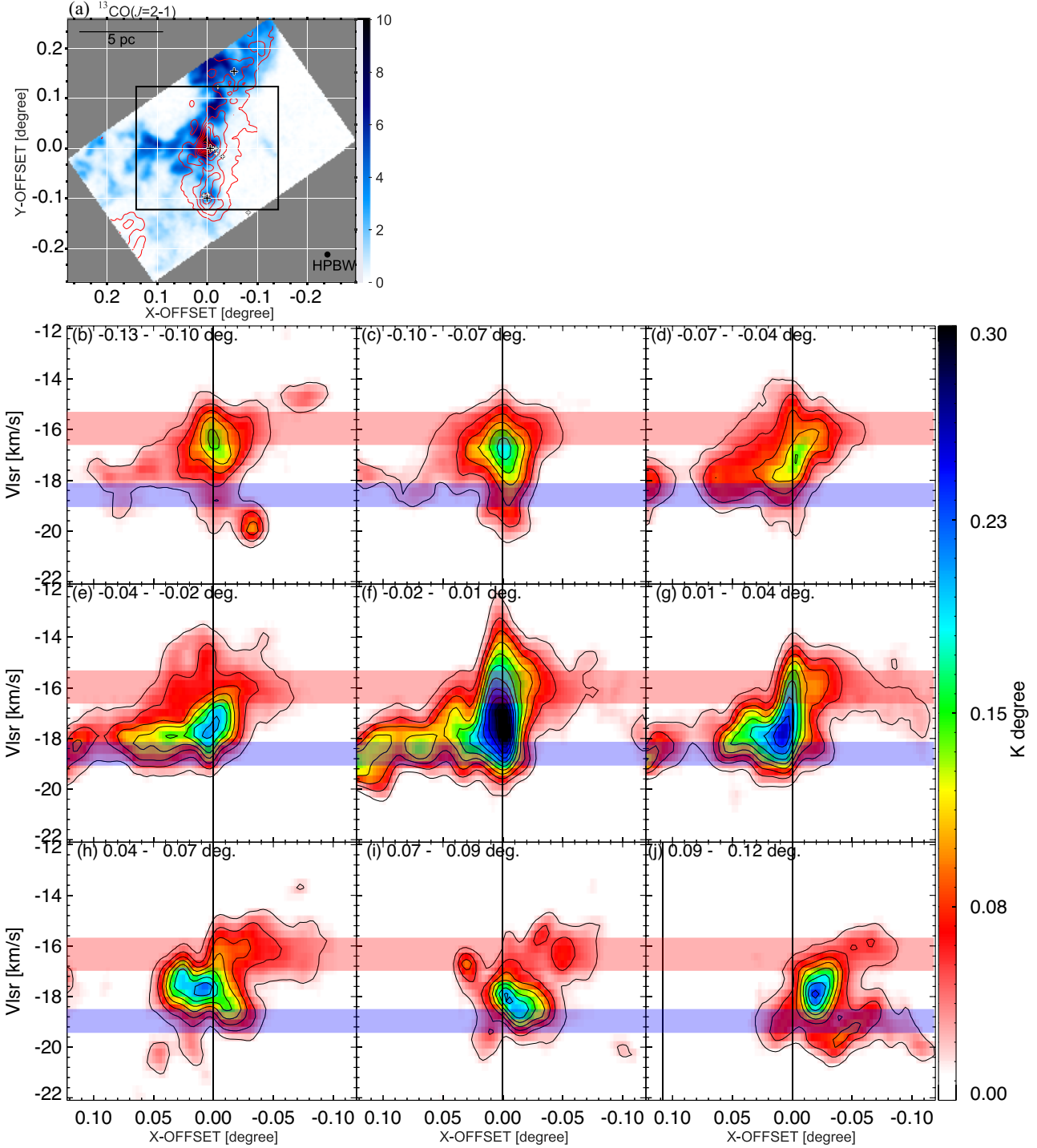


Figure 9. (a) Same as Fig. 6 but in the X-OFFSET and Y-OFFSET coordinate. The X-OFFSET–Y-OFFSET coordinate is defined by rotating the equatorial coordinate (J2000) counterclockwise by 45 deg. The black box indicates the region we present X-OFFSET–velocity channel distributions in (b) to (j). The black crosses and white crosses are the same as Fig. 1. (b)–(j) X-OFFSET–velocity diagrams integrated in the Y-OFFSET intervals of 0.25 deg from a Y-OFFSET of -0.13 deg to 0.12 deg. Contours are plotted every 0.03 K deg from 0.02 K deg.

IRAS source (IRAS05351+3549) (Casoli et al. 1986; Wouterloot & Brand 1989) and no masers (Wouterloot & Brand 1989; Wouterloot, Brand & Fiegle 1993; Bronfman, Nyman & May 1996). Jiang, Wang & Yang (2000) reported outflow toward the source, but no CO wing profile was shown. The core has loose connection to the present collision and requires to be confirmed.

The column densities towards the two cores are $(1-2) \times 10^{22} \text{ cm}^{-2}$ at several times 0.1 pc, and they are forming at least a single high-mass star in each core. This is consistent with the statistics of other ~ 50 cloud–cloud collision objects compiled by Enokiya et al. (2021a) and Fukui et al. (2020b), where a column density of over 10^{23} cm^{-2} and a collision velocity of $\sim 10 \text{ km s}^{-1}$ are the typical

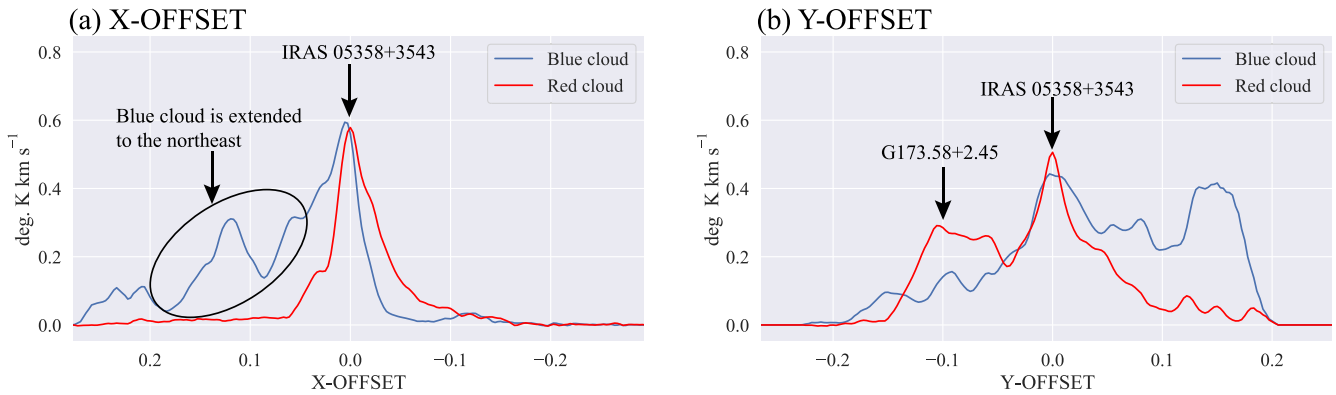


Figure 10. (a) Intensity profile in X-OFFSET integrated from -0.05 deg to 0.05 deg in Y-OFFSET on Fig. 9(a). The profiles of the red and blue clouds are plotted in red and black, respectively. (b) Same as (a) but in Y-OFFSET integrated from -0.05 to 0.05 deg along X-OFFSET on Fig. 9(a).

conditions to form more than 10 OB stars, and a column density of 10^{22} cm^{-2} and a collision velocity of a few km s^{-1} are the conditions to form a single OB star.

4.3 A cloud–cloud collision which provided the initial condition for high-mass star formation

The column density above in IRAS 05358+3543 is close to 10^{22} cm^{-2} at 1 pc scale. It is shown that the column density becomes as high as 10^{23} cm^{-2} at 0.1 pc scale (Beuther et al. 2002). Such physical conditions, the high column density of IRAS 05358+3543, W3 Main, the ONC etc., as high as 1 g cm^{-2} at a sub-pc scale, have been referred to as the typical value of the initial mass density up to $100 M_{\odot}$ within a 0.1 pc radius for high-mass star formation in the previous theoretical works (e.g. Krumholz et al. 2009). These studies of the monolithic collapse model assumed such high gas density in a small scale as the initial condition for high-mass star formation, whereas it was not explored how such extremely high density can be achieved. The present results indicate that a cloud–cloud collision is able to realize such a condition via strong gas compression, where the collision may play an essential role of compression. This is consistent with the theoretical results (Inoue & Fukui 2013; Fukui et al. 2020a), and suggests that a cloud–cloud collision is an essential process for a complete scenario of high-mass star formation which encompasses the formation of the massive dense core prior to the collapse. Without a rapid trigger it seems difficult to collect mass to such high column density by avoiding consumption of the gas for low-mass star formation (Inoue et al. 2018; Fukui et al. 2020b).

5 CONCLUSIONS

It is suggested that IRAS 05358+3543 in Sh2-233IR is a promising candidate for a high-mass protostar. The massive and compact dust condensation of a 0.01 pc radius towards IRAS 05358+3543 is considered to be a convincing signature of protostellar nature, whereas the formation mechanism of the condensation remains unexplored so far, leaving incomplete an evolutionary picture of high-mass star formation. In order to obtain a comprehensive evolutionary picture on IRAS 05358+3543 we have analysed the CO $J = 2-1$ data covering more than $5 \text{ pc} \times 5 \text{ pc}$ at ~ 0.5 pc resolution taken with SMT in the Sh2-233 region and obtained the following results:

(i) The new kinematical analysis of the molecular gas based on the CO($J = 2-1$) data revealed significant details of the molecular

gas around IRAS 05358+3543. The molecular gas shows a marked filamentary distribution of 5 pc length with a 1.5 pc width and has a total mass of $1000 M_{\odot}$. We find two ^{13}CO peaks in the filamentary cloud, where the youngest stellar objects with an age of < 2 Myr are associated. The most outstanding dense cloud core is located towards IRAS 05358+3543 and the second densest towards G173.58+2.45.

(ii) The velocity field around the filament, which is elongated in the north-west to south-east direction, shows a significant systematic difference across the filament. The north-eastern part has velocity of -18.6 km s^{-1} with a range of -19.1 to -18.2 km s^{-1} and the south-west has velocity of -15.9 km s^{-1} with a range of -16.5 to -15.4 km s^{-1} . Their velocity difference 2.7 km s^{-1} is significant as compared with the linewidth 1 km s^{-1} in these clouds, and their internal velocity field has an insignificant velocity gradient within ~ 5 arcmin in filament. We find that the two velocity components show complementary distribution with each other and the filamentary cloud is located towards the boundary between the two components. The filamentary cloud shows ^{13}CO intensity significantly enhanced by a factor of a few, where the two clouds are overlapped. Based on these properties, we infer that a collision between the two clouds took place in the northeast–southwest direction, and compressed the gas to form the filament.

(iii) We frame a scenario that the cloud–cloud collision triggered the formation of the two dense cores in the filament and the young stellar objects therein. We find a discontinuous velocity jump towards the filament, a possible trace of the collisional merging. There is additional velocity broadening due to the protostellar outflow in IRAS 05358+3543, which is not affecting the velocity gap significantly. The time-scale of the collision is estimated to be $(5-8) \times 10^5$ yr by a ratio of the filamentary width 1.5 pc and the velocity difference for a range of the assumed angle $30-60$ deg between the collision velocity and the sightline.

(iv) The present results indicate that IRAS 05358+3543 is associated with a filamentary cloud, which is elongated from the south-east to the north-west. We identify a dust feature possibly corresponding to this filamentary feature at 1 pc scale in the continuum emission at 1.3 mm. At an even smaller scale, we find a dust emission feature of $100 M_{\odot}$ at 0.1 pc scale. These corresponding features suggest that the protostellar source has been formed as part of the filament by the collisional compression in the present scenario. This is consistent with the numerical simulations of colliding molecular flows. Further, at sub-pc scale, the sub-mm and mm continuum images show dust condensations of 0.01 pc scale in IRAS 05358+3543.

(v) On a pc scale the blue-shifted component shows a secondary filamentary distribution of 5-pc in length nearly perpendicular to the

filament. This feature appears to cross with the filament towards the position of IRAS 05358+3543. If we assume that the elongation provides more enhanced density prior to the collision than elsewhere in the filament, it provides an explanation on the location of the IRAS 05358+3543 core. We also note that the IRAS 05358+3543 core has two star clusters, NE and SW, which are separated by 0.5 pc. G173.58+2.45 is also likely formed by the same trigger in the collision, where the lower density led to the formation of a less massive system with a single cluster. The two objects are found to be associated with molecular outflows with dynamical time-scale of $\sim 10^5$ yr, which agree with the simultaneous onset of triggering by the collision separated by 3 pc. The column density of the two cores is $(1-2) \times 10^{22}$ cm $^{-2}$, and values which meet the criterion for the formation of a single O star triggered by a cloud–cloud collision, according to the statistics of cloud–cloud collision candidates.

(vi) The physical conditions, the high column density of IRAS 05358+3543, W3 Main, M42 etc., as high as 1 g cm $^{-2}$ at a sub-pc scale, have been referred to as the typical value of the initial column density for high-mass star formation in the previous theoretical works. These studies of the monolithic collapse model assumed such high column density in a small scale as the initial condition for high-mass star formation, whereas it was not explained how such extremely high density can be achieved. The present results indicate that a cloud–cloud collision enables us to realize such a condition, indicating that the strong gas compression by a collision is essential for a comprehensive scenario of high mass star formation. It is argued that without a rapid collisional trigger it seems difficult to collect mass to such high column density without first consuming the gas by formation of lower mass stars.

ACKNOWLEDGEMENTS

We are grateful to Akio Taniguchi, for his valuable support during data analysis. We also acknowledge Kazuki Tokuda, Kenta Matsunaga, Mariko Sakamoto, and Takahiro Ohno for useful discussion of this paper. The Heinrich Hertz Submillimeter Telescope is operated by the Arizona Radio Observatory, a part of Steward Observatory at The University of Arizona. This research made use of ASTROPY,² a community-developed core Python package for Astronomy (Astropy Collaboration 2013, 2018). This research made use of APLPY, an open-source plotting package for Python hosted at <http://apipy.github.com>. This work was supported by Japan Society for the Promotion of Science (JSPS) KAKENHI Grant Numbers JP15H05694, JP18K13580, JP19K14758, JP19H05075, JP20K14520, JP20H01945, JP21H01136, JP21H00040, and JP22J22931. R.Y. is a Research Fellow of JSPS.

DATA AVAILABILITY

Links to download all the CO data used in this article are shown in section 4 of Biegging et al. 2016.

REFERENCES

Astropy Collaboration 2013, *A&A*, 558, A33
 Astropy Collaboration 2018, *AJ*, 156, 123
 Beuther H., Henning T., Linz H., Krause O., Nielbock M., Steinacker J., 2010, *A&A*, 518, L78
 Beuther H., Leurini S., Schilke P., Wyrowski F., Menten K. M., Zhang Q., 2007, *A&A*, 466, 1065

²<http://www.astropy.org>

Beuther H., Schilke P., Gueth F., McCaughrean M., Andersen M., Sridharan T. K., Menten K. M., 2002, *A&A*, 387, 931
 Biegging J. H., Patel S., Peters W. L., Toth L. V., Marton G., Zahorec S., 2016, *ApJS*, 226, 13
 Bronfman L., Nyman L. A., May J., 1996, *A&AS*, 115, 81
 Carey S. J. et al., 2009, *PASP*, 121, 76
 Casoli F., Dupraz C., Gerin M., Combes F., Boulanger F., 1986, *A&A*, 169, 281
 Chakraborty A., Ojha D. K., Anandarao B. G., Rengarajan T. N., 2000, *A&A*, 364, 683
 Colzi L., Fontani F., Caselli P., Leurini S., Bizzocchi L., Quiaia G., 2019, *MNRAS*, 485, 5543
 Dewangan L. K., Ojha D. K., 2017, *ApJ*, 849, 65
 Dickman R. L., 1978, *ApJS*, 37, 407
 Draine B. T. et al., 2007, *ApJ*, 663, 866
 Draine B. T., 2003, *ARA&A*, 41, 241
 Elmegreen B. G., Lada C. J., 1977, *ApJ*, 214, 725
 Enokiya R. et al., 2021b, *PASJ*, 73, S256
 Enokiya R., Torii K., Fukui Y., 2021a, *PASJ*, 73, S75
 Evans N. J. I., Blair G. N., 1981, *ApJ*, 246, 394
 Fujita S. et al., 2021a, *PASJ*, 73, S172
 Fujita S. et al., 2021b, *PASJ*, 73, S201
 Fukui Y. et al., 2018, *ApJ*, 859, 166
 Fukui Y., Habe A., Inoue T., Enokiya R., Tachihara K., 2020b, *PASJ*, 73, S405
 Fukui Y., Inoue T., Hayakawa T., Torii K., 2021, *PASJ*, 73, S405
 Fukui Y., Tsuge K., Sano H., Bekki K., Yozin C., Tachihara K., Inoue T., 2017, *PASJ*, 69, L5
 Ginsburg A. G., Bally J., Yan C.-H., Williams J. P., 2009, *ApJ*, 707, 310
 Hunter D. A., Massey P., 1990, *AJ*, 99, 846
 Inoue T., Fukui Y., 2013, *ApJ*, 774, L31
 Inoue T., Hennebelle P., Fukui Y., Matsumoto T., Iwasaki K., Inutsuka S.-i., 2018, *PASJ*, 70, S53
 Jessop N. E., Ward-Thompson D., 2000, *MNRAS*, 311, 63
 Jiang Z.-b., Wang M., Yang J., 2000, *Chinese Astron. Astrophys.*, 24, 315
 Kohno M. et al., 2021, *PASJ*, 73, S129
 Kondo H. et al., 2021, *ApJ*, 912, 66
 Krumholz M. R., Klein R. I., McKee C. F., Offner S. S. R., Cunningham A. J., 2009, *Science*, 323, 754
 Ladeyschikov D. A., Sobolev A. M., Parfenov S. Y., Alexeeva S. A., Biegging J. H., 2015, *MNRAS*, 452, 2306
 Larionov G. M., Val'ts I. E., Winnberg A., Johansson L. E. B., Booth R. S., Golubev V. V., 1999, *A&AS*, 139, 257
 Leurini S., Beuther H., Schilke P., Wyrowski F., Zhang Q., Menten K. M., 2007, *A&A*, 475, 925
 Marton G., Tóth L. V., Paladini R., Kun M., Zahorec S., McGehee P., Kiss C., 2016, *MNRAS*, 458, 3479
 McKee C. F., Tan J. C., 2003, *ApJ*, 585, 850
 Megeath S. T., Townsley L. K., Oey M. S., Tiefert A. R., 2008, in Reipurth B., ed., *Handbook of Star Forming Regions, Volume I: The Northern Sky: Low and High Mass Star Formation in the W3, W4, and W5 Regions*. Astron. Soc. Pac., San Francisco, p. 264
 Neelamkodan N., Tokuda K., Barman S., Kondo H., Sano H., Onishi T., 2021, *ApJ*, 908, L43
 Nishimura A. et al., 2018, *PASJ*, 70, S42
 O'Dell C. R., Muench A., Smith N., Zapata L., 2008, in Reipurth B., ed., *Handbook of Star Forming Regions, Volume I: The Northern Sky: Star Formation in the Orion Nebula II: Gas, Dust, Proplyds and Outflows*. Astron. Soc. Pac., San Francisco, p. 544
 Okamoto R., Yamamoto H., Tachihara K., Hayakawa T., Hayashi K., Fukui Y., 2017, *ApJ*, 838, 132
 Palagi F., Cesaroni R., Comoretto G., Felli M., Natale V., 1993, *A&AS*, 101, 153
 Porras A., Cruz-González I., Salas L., 2000, *A&A*, 361, 660
 Reipurth B., Yan C. H., 2008, in Reipurth B., ed., *Handbook of Star Forming Regions: Volume I, The Northern Sky: Star Formation and Molecular Clouds towards the Galactic Anti-Center*. Astron. Soc. Pac., San Francisco, p. 869

- Rosolowsky E. W., Pineda J. E., Kauffmann J., Goodman A. A., 2008, *ApJ*, 679, 1338
- Sakre N., Habe A., Pettitt A. R., Okamoto T., 2021, *PASJ*, 73, S385
- Sano H. et al., 2021, *PASJ*, 73, S62
- Shepherd D. S., Churchwell E., 1996, *ApJ*, 472, 225
- Shepherd D. S., Watson A. M., 2002, *ApJ*, 566, 966
- Snell R. L., Dickman R. L., Huang Y. L., 1990, *ApJ*, 352, 139
- Takahira K., Shima K., Habe A., Tasker E. J., 2018, *PASJ*, 70, S58
- Takahira K., Tasker E. J., Habe A., 2014, *ApJ*, 792, 63
- Tokuda K. et al., 2020, *ApJ*, 896, 36
- Torii K. et al., 2017, *ApJ*, 835, 142
- Tsuboi M., Kitamura Y., Uehara K., Miyawaki R., Tsutsumi T., Miyazaki A., Miyoshi M., 2021, *PASJ*, 73, S91
- Tsuge K. et al., 2019, *ApJ*, 871, 44
- Tsuge K., Fukui Y., Tachihara K., Sano H., Tokuda K., Ueda J., Iono D., Finn M. K., 2021a, *PASJ*, 73, S35
- Tsuge K., Tachihara K., Fukui Y., Sano H., Tokuda K., Ueda J., Iono D., 2021b, *PASJ*, 73, 417
- Urquhart J. S. et al., 2014, *A&A*, 568, A41
- Varricatt W. P., Davis C. J., Adamson A. J., 2005, *MNRAS*, 359, 2
- Wouterloot J. G. A., Brand J., 1989, *A&AS*, 80, 149
- Wouterloot J. G. A., Brand J., Fiegle K., 1993, *A&AS*, 98, 589
- Wright E. L. et al., 2010, *AJ*, 140, 1868
- Yamada R. I. et al., 2021, *PASJ*, 73, 880
- Zinnecker H., Yorke H. W., 2007, *ARA&A*, 45, 481

APPENDIX A: SEPARATION OF THE TWO VELOCITY COMPONENTS BY MULTI-COMPONENT GAUSSIAN FITTING

Because of the proximity in velocities, the spectra in the Sh2-233 region are often merged, and the velocity ranges of the red- and blue-shifted clouds cannot be defined. We applied a peak-detection

algorithm based on Dendrogram (Rosolowsky et al. 2008) and a multiple component Gaussian fitting to each spectrum. The peak-detection algorithm counts a number of peaks to choose the number of Gaussian components. The algorithm also determines initial guess of the fitting. The procedures are described as follows;

- (i) We count a number of peaks by applying Dendrogram to each spectrum, and adaptively decide the number of Gaussian components in fitting.
- (ii) Linewidths, peak intensities, and peak velocities are obtained by Dendrogram, and used as the initial guesses of the fitting.
- (iii) We fit each spectrum to multiple Gaussian function using the initial guesses.

After the fitting, we reconstructed a new data cube consisting of the fitted profiles (hereafter model data).

Figs A1(a) and (b) show integrated intensity maps of the original and model data, respectively. Intensity levels, as shown by both colour scales and contours, fairly agree with each other. Figs A1(c) and (d) show the first moment map of the original data, and peak velocity map of the model data, respectively. The regions with two or more peaks in the profiles are removed.

The regions having second moment greater than 1.0 km s^{-1} (overlapping region) show good correspondence with the regions having two or more peaks as shown by white or magenta contours in Fig. A2. Actually, more than 90 per cent pixels having two or more peaks are enclosed by the second moment greater than 1.0 km s^{-1} contour, which tend to cover wider region probably due to merging of spectra. This means that if we drop the overlapping region, the first and second moments robustly represent the cloud velocity centroids and linewidths, which justifies our method to determine the representative velocity range of a cloud using the two moment maps.

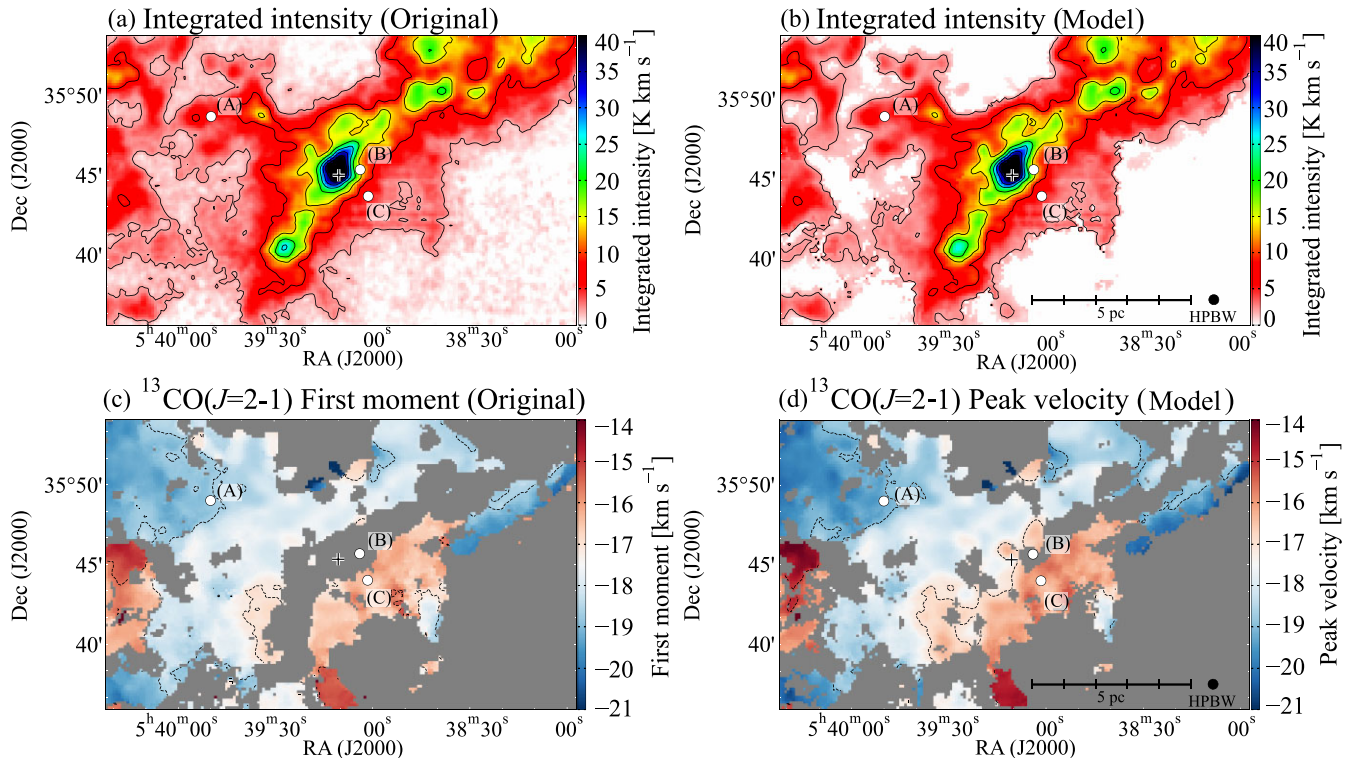


Figure A1. Comparison of the original data and the model data. (a) Same as Fig. 1(b). (b) Integrated intensity distribution of the model data for a velocity range from -22 to -12 km s^{-1} . Contour levels are the same as (a). (c) Same as Fig. 3(a), but contours show -19 and -17 km s^{-1} . (d) Peak velocity map of the model data.

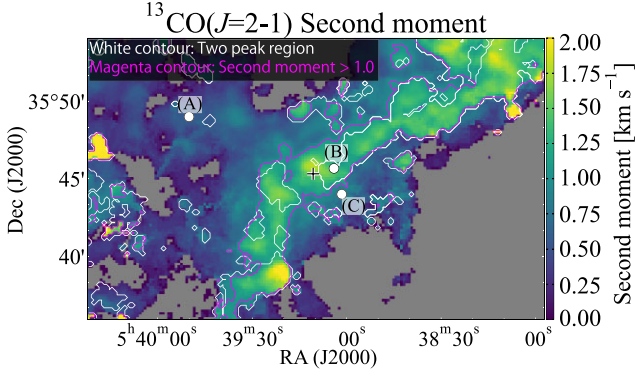


Figure A2. Second moment map of the $^{13}\text{CO}(J = 1-0)$ emission in the Sh2-233 region. The white and magenta contours indicate boundary between single-peaked region and double- or more peaked region. Magenta contours indicate a second moment of 1.0 km s^{-1} .

APPENDIX B: LTE ANALYSES

We derived the column density and mass by assuming the local thermodynamical equilibrium. We used voxels with intensity higher than $6 \times T_{\text{rms}}$ for $^{12}\text{CO}(J = 2-1)$ and $^{13}\text{CO}(J = 2-1)$. Assuming that the $^{12}\text{CO}(J = 2-1)$ emission is optically thick, the excitation temperature T_{ex} of each pixel is derived by

$$T_{\text{ex}} = 11.06 \left\{ \ln \left[1 + \frac{11.06}{T_{\text{peak}} + 0.19} \right] \right\}^{-1}. \quad (\text{B1})$$

The equivalent brightness temperature $J(T)$ is obtained by

$$J(T) = \frac{h\nu}{k_{\text{B}}} \left[\exp \left(\frac{h\nu}{k_{\text{B}}T} \right) - 1 \right]^{-1}, \quad (\text{B2})$$

where h , k_{B} , ν are the Planck constant, Boltzmann constant, and observing frequency. From the radiation transfer equation, the optical depth (τ) of the $^{13}\text{CO}(J = 2-1)$ emission is given by

$$\tau(\nu) = -\ln \left[1 - \frac{T_{\text{mb}}}{J(T_{\text{ex}}) - J(T_{\text{bg}})} \right]. \quad (\text{B3})$$

Using τ , the column density of ^{13}CO is shown by the following equation:

$$N = \sum_{\nu} \tau(\nu) \Delta \nu \frac{3k_{\text{B}}T_{\text{ex}}}{4\pi^3 \nu \mu^2} \exp \left(\frac{h\nu J}{2k_{\text{B}}T_{\text{ex}}} \right) \times \frac{1}{1 - \exp(-h\nu/k_{\text{B}}T_{\text{ex}})}. \quad (\text{B4})$$

Substituting $k_{\text{B}} = 1.38 \times 10^{-16} \text{ (erg K}^{-1}\text{)}$, $\nu = 2.20 \times 10^{11} \text{ (Hz)}$, $\mu = 1.10 \times 10^{-19} \text{ (esu cm)}$, $h = 6.63 \times 10^{-27} \text{ (erg s)}$, $J = 1$, and T_{ex} values of each pixel, we get the column density of H_2 molecule by assuming an abundance ratio to H_2 of ^{13}CO as 5×10^5 (Dickman 1978). The mass of molecular clouds is described as

$$M = m_{\text{p}} \mu_{\text{m}} D^2 \Omega \sum_i N_i(\text{H}_2), \quad (\text{B5})$$

where μ_{m} , m_{p} , D , Ω , and $N_i(\text{H}_2)$ are mean molecular weight, proton mass, distance, solid angle subtending a size of the pixel, and the column density of molecular hydrogen for the i th pixel, respectively. We assume the Helium abundance of 20 per cent, corresponding to a mean molecular weight of 2.8, and a distance of 1.8 kpc.

APPENDIX C: DERIVING PHYSICAL PARAMETERS OF THE MOLECULAR CORES

Figs C1(a) and (b) show closed-up column density maps towards IRAS 05358+3543 and G173.58+2.45 with masses of $230 M_{\odot}$ and $100 M_{\odot}$, respectively. The overlaid contour indicates the half of the peak column density, and we summed the column density over the enclosed area to obtain the mass of the IRAS 05358+3543 core. The G173.58+2.45 core is elongated along the Y-OFFSET axis with a dip in Y-OFFSET-column density profile at Y-OFFSET = $-0:076$. The area above the horizontal line at (X-OFFSET, Y-OFFSET) = $(0:0, -0:06)$ is excluded for deriving the enclosed mass of the G173.58+2.45 core.

We defined the sizes of the cores as an effective radius $r_{\text{eff}} = \sqrt{A/\pi}$, where A indicates the surface area of a cloud.

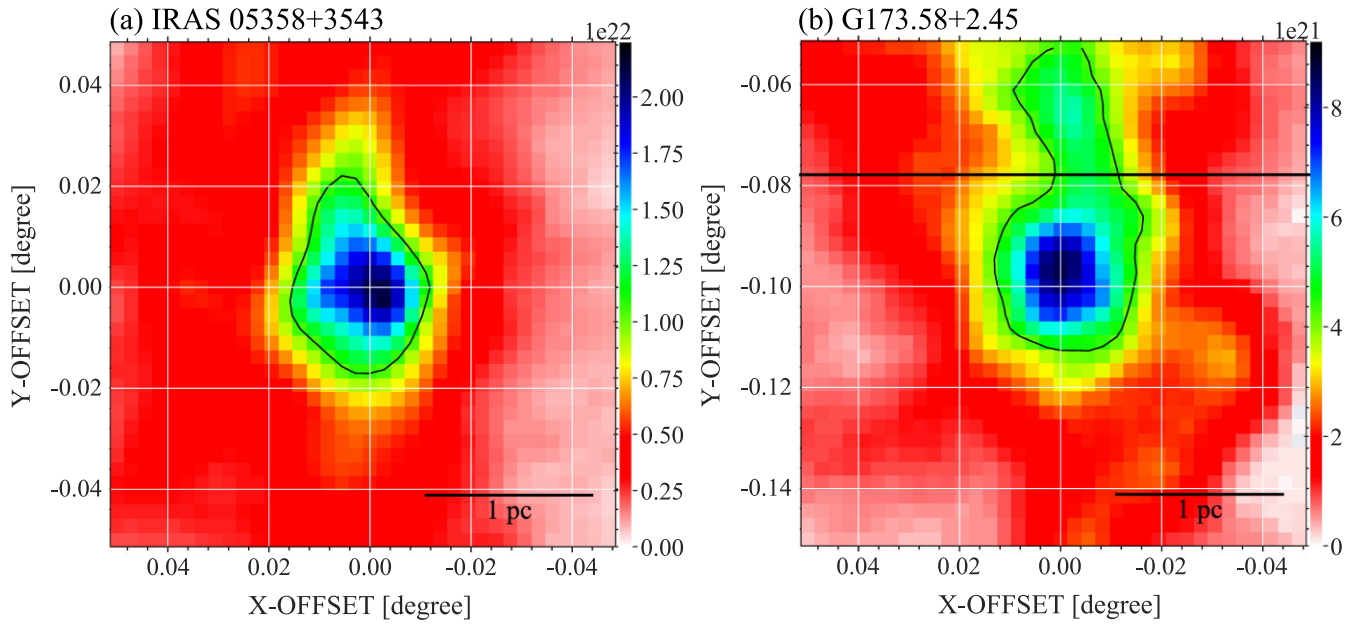


Figure C1. Close-up view of the column density map of IRAS 05358+3543. Superposed contour indicates the half of the peak column density. (b) Same as (a), but for the G173.58+2.45 core. Superposed contour indicates the half of the peak column density. The black horizontal line indicates a Y-OFFSET of -0.076 deg, corresponding to the intensity dip of the Y-OFFSET-intensity profile at X-OFFSET = 0.

This paper has been typeset from a $\text{\TeX}/\text{\LaTeX}$ file prepared by the author.